Int. J. Solids Structures Vol. 29, No. 14/15, pp. 1729–1736, 1992
Printed in Great Britain.

0020–7683/92 $5.00 + .00
Pergamon Press plc

PENETRATION OF 7075-T651 ALUMINUM TARGETS WITH OGIVAL-NOSE RODS

M. J. FORRESTAL and V. K. LUK
Sandia National Laboratories, Albuquerque, NM 87185, U.S.A.

and

Z. ROSENBERG and N. S. BRAR
University of Dayton Research Institute, Dayton, OH 45469, U.S.A.

Abstract—We developed analytical models that predicted forces and penetration depths for long, rigid rods with ogival noses and rate-independent, strain-hardening targets. To verify our models, we conducted terminal-ballistic experiments with 7.1 mm diameter, 0.025 kg, 3.0 caliber-radius-head, ogival-nose rods and 152 mm diameter, 7075-T651 aluminum cylindrical targets. The model predicted penetration depths in good agreement with the data for impact velocities between 370 and 1260 m s^{-1}.

INTRODUCTION

In a recent paper, Forrestal *et al.* (1988) developed penetration equations for rigid projectiles that penetrated rate-independent, elastic, perfectly plastic targets. Subsequently, Kawahara (1986) developed a uniaxial compression test for ductile metals to obtain stress–strain data to 100% true-strain. To provide a more realistic material description for the targets, we modified the penetration equations of Forrestal *et al.* (1988) to include a post-yield, strain-hardening material description. In particular, we obtained stress–strain data for the 7075-T651 targets and approximated the post-yield, stress–strain curve with a power-law data-fit. To verify our penetration equations, we conducted terminal-ballistic experiments with 7.1 mm diameter, 0.025 kg, 3.0 caliber-radius-head, ogival-nose rods and 152 mm diameter, 7075-T651 aluminum cylindrical targets.

The next sections develop the penetration equations, describe the experiments, and compare predicted and measured penetration depths for impact velocities between 370 and 1260 m s^{-1}.

PENETRATION EQUATIONS

Rigid, long-rod projectiles with ogival noses impact a uniform target at normal incidence with velocity V_0 and penetrate at rigid-body velocity V_r. As shown in Fig. 1, an ogive is the arc of a circle tangent to the shank. It is common to define the ogive in terms of caliber-radius-head

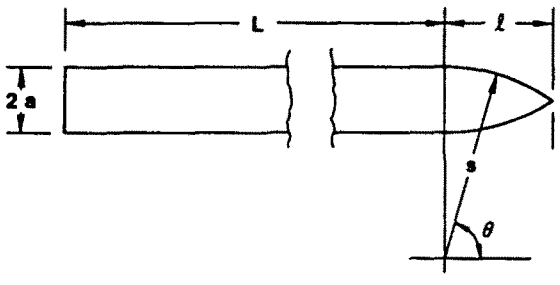

Fig. 1. Projectile geometry.

$$CRH = s/2a = \psi \tag{1a}$$

where s and a are defined in Fig. 1. Also, the nose length is given by

$$l = a(4\psi - 1)^{1/2}. \tag{1b}$$

Post-test, X-ray photographs (Fig. 2) show that the projectiles produced a tunnel in the target about the size of the shank diameter. Forrestal *et al.* (1988, 1991) obtained similar results. In addition, Forrestal *et al.* (1988) took photomicrographs of the post-test targets and showed that a 5–15 μm film on the tunnel surface had undergone microstructural changes. From these observations, we inferred that there was a film of melted target material at the interface between the nose and target during penetration. Thus, we take penetration resistance to consist of stresses normal to the nose and a tangential, frictional component from the melted film. We assume that the tangential stress on the nose σ_t is proportional to the normal stress σ_n, so

$$\sigma_t = \mu\sigma_n \tag{2}$$

where μ is the coefficient of sliding friction.

From Forrestal *et al.* (1988), axial force on an ogival nose is given by

$$F_z = 2\pi s^2 \int_{\theta_0}^{\pi/2} \left\{\left[\sin\theta - \left(\frac{s-a}{s}\right)\right](\cos\theta + \mu\sin\theta)\right\}\sigma_n(V_z, \theta)\,\mathrm{d}\theta \tag{3a}$$

$$\theta_0 = \sin^{-1}\left(\frac{s-a}{s}\right) \tag{3b}$$

where $\sigma_n(V_z, \theta)$ is the normal stress on the ogival nose and the geometric variables are defined in Fig. 1. The normal stress $\sigma_n(V_z, \theta)$ is approximated by results from a spherically symmetric, cavity-expansion analysis (Luk *et al.*, 1991). For this cavity-expansion problem, a spherically symmetric cavity is expanded from zero initial radius at constant velocity V. The material description for this cavity-expansion analysis is elastic, power-law strain-hardening.

Figure 3 shows the compression test data and post-yield data-fit for the 7075-T651 aluminum targets. Young's modulus E, Poisson's ratio ν, yield stress Y, strain-hardening exponent n, and density ρ_t are given. From the material properties in Fig. 3 and the procedures derived by Luk *et al.* (1991), we calculated the radial stress at the cavity surface. Figure 4 shows the radial stress σ_r at the cavity surface versus cavity-expansion velocity V for incompressible and compressible material models.

The spherically symmetric, cavity-expansion results in Fig. 4 can be expressed in the form

$$\sigma_r/Y = A + B[(\rho_t/Y)^{1/2}V]^2 \tag{4}$$

where A and B depend only on material properties. For an incompressible material (Luk *et al.*, 1991)

$$A = \frac{2}{3}\left[1 + \left(\frac{2E}{3Y}\right)^n I\right], \quad B = 3/2 \tag{5a}$$

$$I = \int_0^{1-(3Y/2E)} \frac{(-\ln x)^n}{1-x}\,\mathrm{d}x \tag{5b}$$

where I is evaluated numerically (Amos, 1988). For the material in Fig. 3, $I = 3.896$ and $A = 4.609$. To obtain closed-form penetration equations for the compressible model that

Fig. 2. Post-test, in-material, X-ray photograph for an ogival-nose rod with impact velocity 1260 m s^{-1} (Shot No. 6-1409). Top crater caused by the pusher plate striking the target.

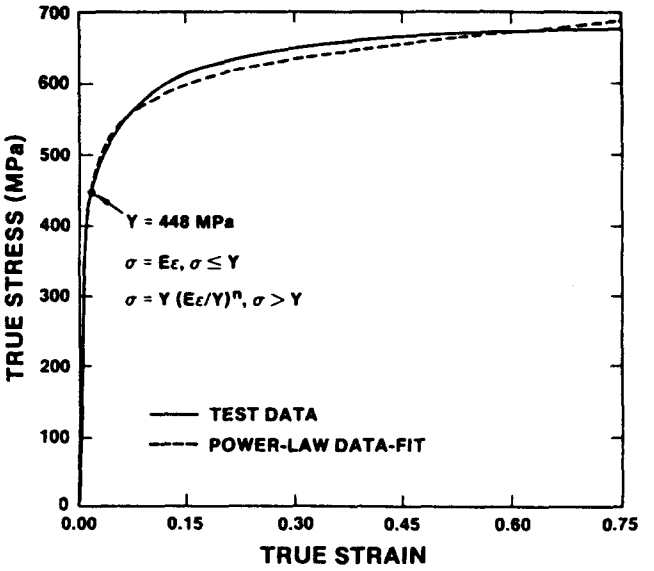

Fig. 3. Compression stress–strain data for the 7075-T651 target material and the power-law data-fit with $E = 73.1$ GPa, $\nu = 0.33$, $Y = 448$ MPa, $n = 0.089$ and $\rho_t = 2710$ kg m^{-3}.

show the geometric and material scales, we curve-fit the spherically symmetric, cavity-expansion results in Fig. 4 with (4). In (4) and Fig. 4, A is the value of σ_r/Y for $V \to 0$, so only B is adjusted to fit the cavity-expansion results. The compressible results in Fig. 4 are curve-fit accurately with $A = 4.418$ and $B = 1.068$.

From the geometry in Fig. 1, the target particle velocity at the nose–target interface caused by the projectile penetrating at rigid-body velocity V_z is

$$v(V_z, 0) = V_z \cos \theta. \tag{6}$$

We approximate the normal stress distribution on the spherical nose σ_n by replacing the

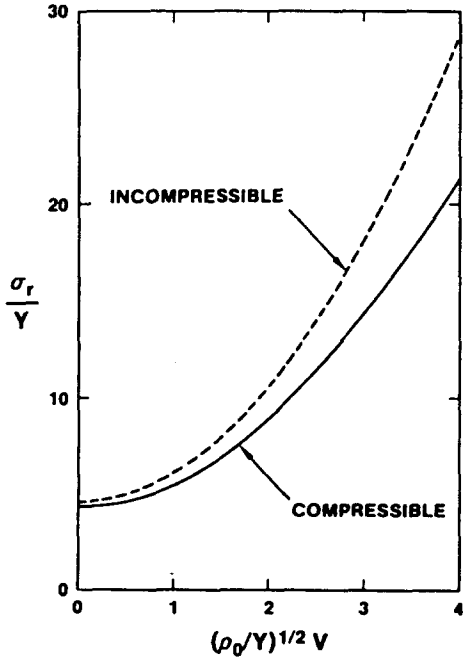

Fig. 4. Radial stress at the cavity surface versus cavity-expansion velocity for an elastic, strain-hardening material. Material properties given in Fig. 3.

spherically symmetric, cavity-expansion velocity V in (4) with the particle velocity v from (6). Thus, normal stress distribution around the spherical nose is taken as

$$\sigma_n(V_z, \theta)/Y = A + B[(\rho_t/Y)^{1/2} V_z \cos\theta]^2. \tag{7}$$

Substitution of (7) into (3a) and integrating gives

$$F_z = \pi a^2 Y(\alpha + \beta \rho_t V_z^2/Y) \tag{8a}$$

$$\alpha = A[1 + 4\mu\psi^2(\pi/2 - \theta_0) - \mu(2\psi - 1)(4\psi - 1)^{1/2}] \tag{8b}$$

$$\beta = B\left[\frac{(8\psi - 1)}{24\psi^2} + \mu\psi^2(\pi/2 - \theta_0) - \frac{\mu(2\psi - 1)(6\psi^2 + 4\psi - 1)(4\psi - 1)^{1/2}}{24\psi^2}\right] \tag{8c}$$

$$\theta_0 = \sin^{-1}\left(\frac{2\psi - 1}{2\psi}\right). \tag{8d}$$

Final penetration depth is obtained from

$$m(\mathrm{d}V_z/\mathrm{d}t) = mV_z(\mathrm{d}V_z/\mathrm{d}z) = -F_z \tag{9}$$

where m is projectile mass and z is penetration depth.

The projectile mass is

$$m = \pi a^2 \rho_p (L + ka) \tag{10a}$$

$$k = (4\psi^2 - 4\psi/3 + 1/3)(4\psi - 1)^{1/2} - 4\psi^2(2\psi - 1)\sin^{-1}\left[\frac{(4\psi - 1)^{1/2}}{2\psi}\right]. \tag{10b}$$

Substitution of (8a) and (10a) into (9) and integrating gives

$$\frac{P}{(L + ka)} = \frac{1}{2\beta}\left(\frac{\rho_p}{\rho_t}\right)\ln\left[1 + \left(\frac{\beta}{\alpha}\right)\left(\frac{\rho_t V_0^2}{Y}\right)\right] \tag{11}$$

where P is final penetration depth and V_0 is impact velocity. The parameters α and β depend only on the target material properties and the projectile nose geometry.

EXPERIMENTS

Targets

The targets were cut from 152 mm diameter (6.0 in.) 7075-T651 aluminum bars, and target length for each test is given in Table 1. In addition, axial specimens from this bar stock were machined for large-strain compression tests. Two specimens were tested at a strain rate of 10^{-1} s^{-1}. The stress–strain curves were nearly identical, and a test result is shown in Fig. 3. Maiden and Green (1966) performed compression tests on 7075-T6

Table 1. Data summary for rods with $2a = 7.11$ mm, $L = 71.12$ mm, $l = 11.79$ mm and $\psi = 3.0$

Shot number	Mass (g)	V_0 (m s^{-1})	ϕ_1, ϕ_2 (degrees)	P (mm)	Target length (mm)
6-1397	24.8	372	0.4, 0.8	26	127
6-1398	24.7	695	1.9, 1.7	70	127
6-1391	24.8	978	0 , 0	127	178
6-1402	24.7	1067	0.1, 0.7	147	229
6-1409	24.8	1258	1.3, 1.1	209	229

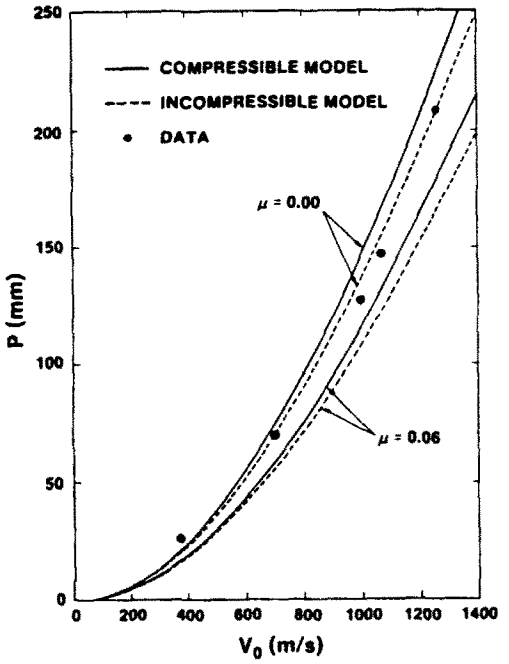

Fig. 5. Predicted and measured final penetration depth.

aluminum for strain rates between 10^{-3} and 10^{3} s^{-1} and showed this material to be strain-rate independent over this range. However, we obtained true strains to 0.75, whereas Maiden and Green (1966) obtained true strains to 0.1. We used the data in Fig. 3 for our target-material model and assumed that the target material was strain-rate independent.

Projectiles

Projectiles (Fig. 1) were machined of T-200 maraging steel† with density $\rho_p = 8020$ kg m^{-3}. The mass, length and diameter for the projectiles are given in Table 1.

Terminal-ballistic experiments

A 20 mm, smooth-bore powder gun launched the rods shown in Fig. 1 to incident velocities between 370 and 1260 m s^{-1}. The rods were encased in two-piece, serrated plastic sabots. Pusher plates were 15.7 mm diameter, 6.35 mm long titanium disks, and the obturator was made of the same material as the sabot. The sabot fit snugly in the gun barrel, while the slightly oversized obturator was forced into the barrel to provide a gas seal. Air drag stripped the sabot, pusher plate and obturator from the rod before impact.

Incident velocity was determined within 1% accuracy by the penetrator interrupting two continuously monitored laser beams, and incident pitch angle ϕ_1 and yaw angle ϕ_2 were measured with X-ray photographs. Definitions of pitch and yaw angles are given by Zukas *et al.* (1982). Post-test penetration depths were measured from in-material X-ray photographs (see Fig. 2). Table 1 summarizes the data for the experimental program. We also conducted an experiment at $V_0 = 1400$ m s^{-1}, but the post-test, in-material, X-ray photograph showed that the shank fractured into several segments.

COMPARISON OF PREDICTED AND MEASURED PENETRATION DEPTHS

Figure 5 shows predictions from the models that take the target material as incompressible and compressible. The target material properties were taken as $E = 73.1$ GPa, $\nu = 0.33$, $Y = 448$ MPa, $n = 0.089$ and $\rho_t = 2710$ kg m^{-3}. Projectile geometries and masses

† Vasco Pacific, 707 West Olympic Blvd., Montebello, CA 90640, U.S.A. T-200 maraging steel has a nominal yield stress of 200 ksi.

(ρ_p = 8020 kg m^{-3}) are given in Fig. 1 and Table 1. In addition, the models require the sliding-interface friction coefficient μ. Forrestal *et al.* (1988) discuss experiments that determine μ at fast, sliding velocities. Unfortunately, values of μ are apparatus-dependent and vary between 0.02 and 0.20. For Fig. 5, we used $\mu = 0$ and $\mu = 0.06$.

The predictions in Fig. 5 show that the models are more sensitive to the selection of the sliding friction coefficient than to the effect of compressibility. In addition, the predictions bracket the data for μ equal to 0 to 0.06.

SUMMARY AND CONCLUSIONS

We developed an analytical model that predicted penetration depth for long, rigid rods with ogival noses and rate-independent, strain-hardening targets. The spherical, cavity-expansion approximation simplified the target analysis, so we obtained closed-form penetration equations that showed the geometric and material scales. Data from the terminal-ballistic experiments were in good agreement with model predictions. Any improvements in modeling will require new experimental methods that quantify the sliding frictional resistance between the projectile and target.

Acknowledgements—This work was supported by the U.S. Department of Energy. The authors thank W. A. Kawahara for the data in Fig. 3.

REFERENCES

Amos, D. E. (1988). Evaluation of integrals related to the Debye function. SAND88-2896, Sandia National Laboratories, Albuquerque, New Mexico.

Forrestal, M. J., Okajima, K. and Luk, V. K. (1988). Penetration of 6061-T651 aluminum targets with rigid long rods. *J. Appl. Mech.* **55**, 755–760.

Forrestal, M. J., Brar, N. S. and Luk, V. K. (1991). Penetration of strain-hardening targets with rigid spherical-nose rods. *J. Appl. Mech.* **58**, 7–10.

Kawahara, W. A. (1986). Compression materials testing at low to medium strain rates. Paper No. 86-WA/Mats-15, presented at the ASME Winter Annual Meeting, Anaheim, California.

Luk, V. K., Forrestal, M. J. and Amos, D. E. (1991). Dynamic spherical cavity-expansion of strain-hardening targets. *J. Appl. Mech.* **58**, 1–6.

Maiden, C. J. and Green, S. J. (1966). Compressive strain-rate tests on six selected materials at strain rates from 10^{-1} to 10^{4} in./in./sec. *J. Appl. Mech.* **33**, 496–504.

Zukas, J. A., Nicholas, T., Swift, H. F., Greszczuk, L. B. and Curran, D. L. (1982). *Impact Dynamics*, p. 206. Wiley, New York.